

## Research Article

# Microstructure evolution of nanostructured ferritic alloy with and without $\text{Cr}_3\text{C}_2$ coated SiC at high temperatures

Kaustubh Bawane, Kathy Lu\*

<sup>a</sup> Department of Materials Science and Engineering, Virginia Polytechnic Institute and State University, Blacksburg, Virginia 24061, USA

\*Corresponding author. Prof., Ph.D.; Tel: +1 540 231 3225.

*E-mail address:* klu@vt.edu (K. Lu).

[Received 27 July 2019; Received in revised form 29 September 2019; Accepted 17 October 2019]

This work focuses on fundamental understanding of microstructure evolution of nanostructured ferritic alloy (NFA) and 25 vol.%  $\text{Cr}_3\text{C}_2$  coated SiC( $\text{Cr}_3\text{C}_2$ @SiC)-NFA composite during spark plasma sintering at 950°C and the following thermal treatment at 1000 °C. A unique bi-phase microstructure with distinct Cr-rich and Si-rich phases has been observed for the 25 vol.%  $\text{Cr}_3\text{C}_2$ @SiC-NFA composite, while for the NFA sample, the traditional large grain microstructure remains. Grain sizes are significantly smaller for the 25 vol.%  $\text{Cr}_3\text{C}_2$ @SiC-NFA composite compared to those for the pure NFA, which can be attributed to the presence of grain boundary phases in the composite sample. During the thermal treatment, microstructure features can be directly correlated with the dissolution kinetics and phase diagrams calculated using Thermo-Calc/DICTRA/PRISMA<sup>®</sup>.

*Key words:* Cr<sub>3</sub>C<sub>2</sub> coated SiC; Nanostructured ferritic alloy; Thermal treatment; M<sub>7</sub>C<sub>3</sub> precipitate; Thermo-Calc simulation; Metal matrix composites

## 1. Introduction

The viability of advanced nuclear energy systems strongly depends on the development of new materials that can deliver high performance in aggressive environments at elevated temperatures. Fuel cladding separates radioactive nuclear fuels from coolants. Selection of appropriate materials for cladding plays a critical role in nuclear reactor safety and durability. Currently, all major commercial nuclear reactors (Gen II) use zirconium based alloy (e.g., Zircalloy, ZIRLO, M5, etc.) fuel claddings [1-4]. However, zirconium alloy based claddings are notorious for hydrogen embrittlement and reaction with steam at elevated temperatures, especially during ‘loss of coolant accident (LOCA)’ events [1, 3, 4]. Numerous materials such as ferritic steels [5-7], ferritic-martensitic steels [8-10], ODS alloys [11-13], austenitic stainless steels [1, 4], SiC [14-17], and nickel based alloys [1, 2, 4] are being studied to replace zirconium alloy based claddings in order to achieve higher nuclear reactor safety and efficiency for Gen II and Gen III light water reactors, as well as to be used as new cladding materials in the proposed Gen IV reactors to withstand a nuclear exposure dose of 50-150 dpa at 550-1000 °C [3, 6, 7, 14, 16-18]. Nanostructured ferritic alloys (NFAs), a special type of oxide dispersion strengthened (ODS) ferritic steels, are being considered as a promising nuclear cladding material for both nuclear fission and fusion reactor systems [13, 19-21]. The combination of desirable properties, such as resistance to high temperature corrosion, irradiation, void swelling, and creep as well as high temperature strength makes NFAs very attractive for nuclear applications [3, 7, 22, 23].

Silicon carbide (SiC) is being widely considered as another desirable cladding material for nuclear reactors. It exhibits high irradiation resistance, excellent high temperature strength,

slow oxidation kinetics, and high chemical stability [15, 24-27]. SiC and its composites are being intensively studied for their use in fusion reactors, LWR fuel claddings [28-30], and high temperature gas reactors [30-32]. They are stable and effective against irradiation as nuclear reactor structural components.

Spark plasma sintered NFA and SiC-NFA composites with and without reaction barriers ( $\text{Cr}_3\text{C}_2$  and carbon) were explored in our previous research [33-36] for nuclear reactor claddings. A  $\text{Cr}_3\text{C}_2$  coating on SiC particles ( $\text{Cr}_3\text{C}_2@\text{SiC}$ ) and a carbon coating on NFA ( $\text{C}@\text{NFA}$ ) particles were created in order to suppress the formation of detrimental reaction products such as iron silicides ( $\text{Fe}_3\text{Si}$ ,  $\text{FeSi}$ ) [35, 36]. Our earlier work reported density, hardness, and preliminary microstructural characterization of spark plasma sintered (SPS)  $\text{Cr}_3\text{C}_2@\text{SiC}$ -NFA composites with various  $\text{Cr}_3\text{C}_2@\text{SiC}$  volume fractions. These composites showed excellent mechanical and high temperature oxidation and irradiation properties [36-39]. With combined properties of NFA and SiC, they can serve as a promising candidate for fuel cladding to replace existing zirconium based alloys.

This work reports detailed microstructural characterization and comparison of the pure NFA and  $\text{Cr}_3\text{C}_2@\text{SiC}$ -NFA composite after the SPS sintering. Microstructural evolution during prolonged thermal treatment at 1000°C is also discussed. Phase evolution and precipitate formation are evaluated using Thermo-Calc/DICTRA/PRISMA simulations.

## **2. Materials and methods**

The NFA powder was prepared using high energy ball milling of a ferritic steel powder (Fe-9Cr-2W-0.4Ti-0.2V-0.18C) with 0.3 wt%  $\text{Y}_2\text{O}_3$  in an argon atmosphere (average size ~15  $\mu\text{m}$ , ball milling was performed at Oak Ridge National Laboratory). SiC particles (Grade UF-15,  $\alpha$ -SiC, ~1.25  $\mu\text{m}$  average size, H.C. Starck, Karlsruhe, Germany) were coated with  $\text{Cr}_3\text{C}_2$  using a

melt salt method followed by reduction treatment at high temperatures. The NFA and 25 vol.%  $\text{Cr}_3\text{C}_2@\text{SiC}$  powder were mixed and densified using spark plasma sintering (SPS) at 950 °C with a heating/cooling rate of 50 °C/min, applied pressure of 100 MPa, and holding time of 10 min. Detailed procedures of creating the  $\text{Cr}_3\text{C}_2$  coating on SiC and sintering the pure NFA and  $\text{Cr}_3\text{C}_2@\text{SiC}$ -NFA composite were reported in our previous work [36].

The SPS densified NFA and 25 vol.%  $\text{Cr}_3\text{C}_2@\text{SiC}$ -NFA composite were treated at 1000°C in an argon atmosphere for 50 hours. The thermal treatment was performed in a tube furnace (1730-20 HT Furnace, CM Furnace Inc., Bloomfield, NJ) with a gas flow of ~1.2 L min<sup>-1</sup> at 1 atm pressure.

Microstructures were analyzed using scanning electron microscopy in the backscattered mode (FEG E-SEM QUANTA600, FEI Company, Hillsboro, OR, USA) and the compositions were analyzed using energy dispersive spectroscopy (Bruker EDS). An electron backscatter diffraction detector (TSL/EDAX/EBSD attached to a focused ion beam microscope (FIB), Helios Nanolab, FEI Company, Hillsboro, OR, USA) was used to characterize grain size and grain size distribution. The EBSD measurements were performed using a 20 kV beam (probe current = 11 nA) with a 70° tilt angle to the horizontal axis. The EDAX Team software was used to collect data and the OIM analysis software was used for post processing and data analysis without the problem of interconnecting grains. EBSD maps were cleaned using grain dilation routing with default parameters (grain tolerance angle ~5° and minimum grain size ~2 pixels).

STEM-EDS analysis was performed using scanning transmission electron microscopy (JEOL 2100 attached with an EDS detector). The samples for the STEM-EDS analysis were obtained by cutting a thin sample section (~400 μm) using a Beuhler Isomet low speed saw. The section was then gently polished with diamond papers (~1 μm size) up to ~60 μm thickness.

Final thinning was carried out using a Fischione 1010 low angle ion mill under a 3 kV argon ion beam, a 5 mA current, and a 12° incident angle. The JEOL TEM was also used to acquire electron diffraction patterns from various phases. CrystalMaker and CrysTBox software packages were used for phase identification based on diffraction pattern analysis.

ThermoCalc® software was used to calculate the phase diagram of the NFA and SiC system. The Si and C elements were simultaneously varied in the same amount in the NFA alloy to mimic addition of SiC. The DICTRA module in ThermoCalc was used to simulate the dissolution of spherical SiC particles in NFA at the sintering temperature of 950 °C. Diffusion profiles of important elements (Fe, Cr, Si, and C) were plotted against the distance from the SiC-NFA interface to estimate the amount of SiC dissolution. Finally, the formation of new precipitates and their sizes after sintering and thermal treatment were estimated using TTT diagram and PRISMA module in ThermoCalc. The Y and O elements were not considered for simulation because Y-rich nanoclusters should have formed much before the dissolution of Cr<sub>3</sub>C<sub>2</sub>@SiC in NFA owing to the supersaturation (of Y and O in NFA) during mechanical alloying itself. Since SiC dissolved into the NFA very fast and the amount was much higher (25 vol.%) than the Y<sub>2</sub>O<sub>3</sub> content (0.3 wt%), the impact of the Y<sub>2</sub>O<sub>3</sub> nanoclusters in the SiC dissolution was ignored. TCFE9 and MOBFE4 databases were used for all these calculations.

### **3. Results and discussion**

#### *3.1. Microstructural evolution during spark plasma sintering*

Fig. 1 shows the SEM micrographs of the spark plasma sintered NFA and 25 vol.% Cr<sub>3</sub>C<sub>2</sub>@SiC-NFA samples. The NFA sample shows mainly equiaxed grains along with some pores at the grain boundaries; there are no visible secondary phases, as indicated in Fig. 1(a). The microstructure of the 25 vol.% Cr<sub>3</sub>C<sub>2</sub>@SiC-NFA sample shows fine light gray precipitates (P1)

in a dark gray matrix as shown in Fig. 1(b). The precipitates (P1) form interconnected structures, possibly due to their large volume fraction and coalescence of adjacent growing precipitates during the spark plasma sintering process. Very fine and bright precipitates (P2) can also be seen throughout the microstructure (Fig. 1(b)). The dark phase (pointed out by the green arrow) in Fig. 1(b) is a graphite precipitate as identified in our previous work [36]. The P1 and P2 precipitates are identified as  $M_7C_3$  and  $MC$  type carbides and will be discussed in detail in Section 3.2. All these precipitates, P1, P2, and graphite, are a result of reactions between the NFA and  $Cr_3C_2@SiC$  particles during the spark plasma sintering, as to be discussed in Section 3.3. It should be mentioned that Y-Ti-O-rich precipitates (or clusters) are present in the NFA and 25 vol.%  $Cr_3C_2@SiC$ -NFA samples. However, they are too fine to be visible in these images. Previous studies on various ODS/NFA alloys have shown that very fine (2-4 nm) Y-rich nanoclusters (such as Y-Ti-O) are only visible from high magnification TEM images with certain imaging conditions or using atom probe tomography. Examples are the work of Massey et al. [40], which showed no oxide clusters under TEM and EDS but the opposite through atom probe tomography, as well as Kishimoto et al.'s [41] work on 14CrYWTi alloy, which showed no oxide clusters in a low magnification bright field TEM image, but with dark field imaging under high magnification showed the presence of the nanoclusters. Since Y-Ti-O nanoclusters are not the focus of this study, these experiments were not performed. Previous research on the same NFA alloy has reported the presence of 2-4 nm Y-Ti-O nanoclusters with a high number density ( $\sim 10^{24} m^{-3}$ ). Recent work on spark plasma sintered 9Cr [42] and 14Cr [43, 44] ODS alloys have reported fine Y-Ti-O nanoclusters in the microstructures. It is fair to assume that both NFA and  $Cr_3C_2@SiC$ -NFA composites reported here contain fine Y-Ti-O nanoclusters. In addition,

extensive studies on the functions of these clusters have been carried out before<sup>[45, 46]</sup> and will not be discussed here.

Fig. 2(a) shows the EBSD inverse pole figure (IPF) map of the SPS sintered NFA specimen. The grain size is on average  $\sim 15 \mu\text{m}$  but the microstructure has a mixture of very large grains ( $\sim 45 \mu\text{m}$ ) and plenty of small grains ( $4\text{-}5 \mu\text{m}$ ). Such a bimodal grain size distribution has been previously observed in various SPS sintered ODS alloys<sup>[42, 47-54]</sup>. The behavior is attributed to variations in dislocation density and heterogeneous distribution of Y-Ti-O nanoclusters, which create heterogeneous grain boundary pinning effects and also local variations in heat distribution due to the joule heating effect during the SPS process<sup>[48, 53, 55]</sup>. The IPF map in Fig. 2(a) shows no preferential grain orientation and almost fully recrystallized grains with no remnants of dendritic microstructures from the starting powder. Fig. 2(b) and (c) shows the IPF maps of  $\alpha$ -ferrite and  $M_7C_3$  grains of the 25 vol.%  $\text{Cr}_3\text{C}_2@\text{SiC}$ -NFA composite respectively. There is no preferential grain orientation for the  $\alpha$ -ferrite grains. The size of the  $\alpha$ -ferrite grains is much smaller ( $\sim 3 \mu\text{m}$ ) compared to that of the NFA sample ( $\sim 15 \mu\text{m}$ ). The overall smaller size grains in the 25 vol.%  $\text{Cr}_3\text{C}_2@\text{SiC}$ -NFA composite can be attributed to the strong pinning effect due to the significant precipitation of the P1 and P2 phases as a result of the reactions between NFA and  $\text{Cr}_3\text{C}_2@\text{SiC}$  during the spark plasma sintering. Fig. 2(c) shows that the interconnected worm-like structure of the  $M_7C_3$  (or P1) precipitates consists of small ( $1\text{-}1.5 \mu\text{m}$ ) sized equiaxed grains with no preferential orientation. Fig. 2(d) shows the EBSD phase map of the 25 vol.%  $\text{Cr}_3\text{C}_2@\text{SiC}$ -NFA composite with the  $\alpha$ -ferrite and  $M_7C_3$  phases. The shape and size of the  $\alpha$ -ferrite and  $M_7C_3$  phases correspond well with the dark gray and light gray regions in the SEM image as shown in Fig. 1(b) respectively.

### 3.2. Effect of thermal treatment on microstructures

Fig. 3 shows the microstructures of the NFA and 25 vol.% Cr<sub>3</sub>C<sub>2</sub>@SiC-NFA composite after the thermal treatment at 1000 °C for 50 h. The NFA sample (Fig. 3(a)) shows equiaxed grains, similar to those observed before the thermal treatment (Fig. 1(a)). The 25 vol.% Cr<sub>3</sub>C<sub>2</sub>@SiC-NFA composite after the treatment (Fig. 3(b)) shows dark gray NFA (ferrite) grains, light gray P1 precipitate, and fine bright P2 precipitate, similar to those before the thermal treatment (Fig. 1(b)). The major change is the grain sizes. Fig. 4 shows the size and volume fraction of the precipitates (P1, P2) before and after the 1000 °C treatment measured using ImageJ software (grey scale method was used for volume fraction measurement). The sizes of the P1 and P2 precipitates show 110% and 108% increases, respectively, after the thermal treatment at 1000 °C. The volume fractions of the P1 and P2 precipitates show 37.5% and 75% increases respectively. Therefore, the thermal treatment at 1000 °C has resulted in significant coarsening and potentially more nucleation of the existing precipitates (P1 and P2). In both cases, the amount of the P2 phase (MC) is significantly less than that of the P1 phase (M<sub>7</sub>C<sub>3</sub>).

Fig. 5 shows the STEM bright field images of the 25 vol.% Cr<sub>3</sub>C<sub>2</sub>@SiC-NFA composite after the thermal treatment at 1000 °C for 50 h. The bright region is Fe-rich (Fig. 5(b)). This phase is similar to the dark grey NFA grains in the corresponding SEM images (Figs. 1(b) and 3(b)). The dark region in Fig. 5 can be correlated with the P1 precipitate in the SEM images in Figs. 1(b) and 3(b). The diffraction patterns corresponding to the bright region (NFA) and dark region (P1) in Fig. 5 are shown in Fig. 6(a) and (b), respectively. The patterns are indexed by comparing with the simulated patterns from the CrysTBox and CrystalMaker™ software packages and Fig. 6(a) and (b) are consistent with standard NFA and M<sub>7</sub>C<sub>3</sub> crystallographic files (.cif files available on the Crystallography Open Database (COD) website). The NFA region has

been indexed as an  $\alpha$ -ferrite phase, while the P1 phase is identified as a  $M_7C_3$  phase, which is consistent with the EBSD results from Fig. 2(c). The EDS mappings in Fig. 5(a) and (b) show that the  $M_7C_3$  phase is rich in both Fe and Cr. Therefore, the composition of the P1 precipitates should be  $(Fe,Cr)_7C_3$ .

Some fine precipitates can be observed in both the bright and dark regions as shown in Fig. 5(a) and (b). This phase is made up of the bright fine precipitates (P2) observed in Fig. 1(b) and 3(b). The EDS analysis shows Ti- and W-enrichment in these precipitates. The W-enrichment explains the bright contrast in the SEM images (Figs. 1(b) and 3(b)). These precipitates are believed to be  $(Ti,W)C$ , i.e.  $MC$  type carbides<sup>[56]</sup>. It should be mentioned that the presence of the  $M_7C_3$  and  $MC$  carbide phases has been previously reported for various ODS and ferritic alloys<sup>[56-59]</sup>. STEM images in Fig. 5 are at low magnification.

### 3.3. Fundamental understanding of microstructural evolution

Fig. 1(b) shows that the spark plasma sintering process has resulted in complete dissolution of the  $Cr_3C_2@SiC$  powder and formation of new phases such as  $(Fe,Cr)_7C_3$ ,  $(Ti,W)C$ , and graphite. The reactions between SiC and NFA after the coating dissolution can be divided into two steps. The first step is dissociation of SiC into Si and C, according to Eq. (1). The dissociated Si and C atoms diffuse into NFA, thus forming Si- and C-containing supersaturated NFA. This supersaturated NFA then leads to the precipitation of graphite,  $M_7C_3$ , and  $MC$  phases as shown in Fig. 1(b).



The dissolution kinetics of SiC has been studied using the DICTRA<sup>®</sup> software package as shown in Fig. 7. Within only 400 s, a significant amount of SiC region has dissolved ( $\sim 4.3 \mu m$  thick) in the NFA at 950 °C. This behavior is driven by the high diffusivities ( $2.37 \times 10^{-13} m^2/s$

and  $1.31 \times 10^{-10}$  m<sup>2</sup>/s) of Si and C respectively in the  $\alpha$ -ferrite matrix. Since the original SiC particle size was around 1-2  $\mu$ m, all the SiC particles should have dissolved in the NFA matrix. Therefore, it can be assumed that supersaturated NFA with homogeneous Si and C compositions has formed at a sintering temperature of 950°C according to Eq. (1). Fig. 8(a-d) shows diffusion behaviors of important elements (Fe, Cr, Si, and C respectively) in this system. The diffusion behavior of Si and C in Fig. 8(b) and (d) clearly shows significant penetration inside the NFA matrix after SiC dissolution (around ~20  $\mu$ m for Si and ~60  $\mu$ m for C).

The second step involves formation of equilibrium phases from the newly homogenized composition. This leads to the precipitation of graphite,  $(\text{Fe,Cr})_7\text{C}_3$ , and  $(\text{Ti,W})\text{C}$  phases according to the reaction in Eq. (2). The phase diagram of the  $\text{Cr}_3\text{C}_2$ @SiC-NFA composite in Fig. 9 confirms the formation of these phases. The precipitation of the secondary phases from the supersaturated NFA can be visualized using the phase diagram in Fig. 9 and the TTT diagram in Fig. 10. It shows the presence of NFA ( $\alpha$ -ferrite with dissolved Si), graphite, and carbides  $(\text{Fe,Cr})_7\text{C}_3$  and  $(\text{Ti,W})\text{C}$ . This observation correlates well with the results from our previous work where Si dissolved  $\alpha$ -ferrite and graphite were observed using SEM-EDS [36]. The phase diagram was constructed using the ThermoCalc console mode, where the  $\text{Cr}_3\text{C}_2$ @SiC content in the NFA was varied rather than only varying a single element. The TTT diagram in Fig. 10 shows that all the precipitates form almost instantaneously ( $<10^{-2}$  s) at 950 °C (during the sintering) as well as during the thermal treatment at 1000 °C.



In Fig. 4, both the size and volume fraction of the  $M_7\text{C}_3$  and  $MC$  type precipitates increase after the 1000 °C thermal treatment. This means that the thermal treatment has resulted in coarsening of the precipitates formed during the SPS sintering along with potential nucleation

of new  $(\text{Fe,Cr})_7\text{C}_3$  and  $(\text{Ti,W})\text{C}$  type precipitates based on the TTT diagram in Fig. 10. Precipitation simulations were carried out at 1000 °C using the PRISMA module of the ThermoCalc software to estimate the size of the  $M_7\text{C}_3$  and  $MC$  carbides after the thermal treatment. The simulated sizes of the  $(\text{Fe,Cr})_7\text{C}_3$  and  $(\text{Ti,W})\text{C}$  type carbides match reasonably well with the experimental results as shown in Fig. 11. Fig. 12(a) and (b) shows the SEM micrographs of the  $\text{Cr}_3\text{C}_2@\text{SiC}$ -NFA composite after the thermal treatment at 1000 °C for 25 and 75 h, respectively. The precipitate sizes after the 25 h and 75 h treatment are also plotted in Fig. 11. The estimated sizes of the  $(\text{Fe,Cr})_7\text{C}_3$  and  $(\text{Ti,W})\text{C}$  type precipitates before the thermal treatment (or after sintering) are much smaller than the actual sizes in Fig. 4. This means local overheating and enhanced diffusion under the electric current in the SPS sintering must have accelerated the nucleation and growth of these precipitates, since the ThermoCalc software cannot consider the electric field effect. This process can be visualized using enhanced mass transport from an electromigration theory in Eq. (3):

$$J_i = -\frac{D_i C_i}{RT} \left[ \frac{RT}{\partial x} \frac{\partial \ln C_i}{\partial x} + F z^* E \right] \quad (3)$$

where  $J_i$  is the flux of the diffusing species  $i$ ,  $D_i$  is the diffusivity of the species,  $C_i$  is the concentration of the species,  $F$  is Faraday's constant,  $z^*$  is the effective charge on the diffusing species,  $E$  is the field,  $R$  is the gas constant, and  $T$  is temperature.

Coarsening of the  $(\text{Fe,Cr})_7\text{C}_3$  and  $(\text{Ti,W})\text{C}$  precipitates can be visualized based on the Ostwald ripening equation:

$$r^3 - r_0^3 = \frac{8\gamma c v^2 D}{9RT} t = kt \quad (4)$$

where  $r$  and  $r_0$  are the radii of the precipitate before and after the thermal treatment, respectively,  $\gamma$  is surface energy,  $c$  is the solubility of the precipitate,  $D$  is the diffusivity of the precipitate,  $v$  is the molar volume of the precipitate,  $t$  is time, and  $k$  is coarsening rate coefficient.

For the  $(\text{Fe,Cr})_7\text{C}_3$  and  $(\text{Ti,W})\text{C}$  precipitates, the coarsening rate coefficient  $k$  can be calculated using the ThermoCalc-DICTRA module as shown in Fig. 13. The estimated sizes of the  $(\text{Fe,Cr})_7\text{C}_3$  precipitates after the 1000 °C treatment for 25, 50 and 75 hours are 1.19  $\mu\text{m}$ , 1.33  $\mu\text{m}$ , and 1.44  $\mu\text{m}$ , while the experimental values are  $1.3\pm 0.3$   $\mu\text{m}$ ,  $2.1\pm 0.4$   $\mu\text{m}$ , and  $2.2\pm 0.5$   $\mu\text{m}$  respectively. Similarly, the estimated sizes of the  $(\text{Ti,W})\text{C}$  precipitates after the 1000°C treatment for 25, 50 and 75 hours are 0.147  $\mu\text{m}$ , 0.181  $\mu\text{m}$ , and 0.205  $\mu\text{m}$ , while the experimental values are  $0.095\pm 0.03$   $\mu\text{m}$ ,  $0.16\pm 0.5$   $\mu\text{m}$ , and  $0.15\pm 0.08$   $\mu\text{m}$  respectively. The simulated sizes of both  $(\text{Fe,Cr})_7\text{C}_3$  and  $(\text{Ti,W})\text{C}$  precipitates are reasonably close to the size range observed during the experiments.

#### 4. Conclusion

Microstructural evolutions of spark plasma sintered NFA and 25 vol.%  $\text{Cr}_3\text{C}_2@ \text{SiC}$ -NFA composite before and after the thermal treatment at 1000 °C for 50 h were studied. The grain sizes for the 25 vol.%  $\text{Cr}_3\text{C}_2@ \text{SiC}$ -NFA composite are far smaller than those for the NFA sample (2  $\mu\text{m}$  vs. 12  $\mu\text{m}$ ). The 25 vol.%  $\text{Cr}_3\text{C}_2@ \text{SiC}$ -NFA composite shows a large amount of  $(\text{Fe,Cr})_7\text{C}_3$  and  $(\text{Ti,W})\text{C}$  carbides in the microstructure along with the  $\alpha$ -ferrite (NFA) matrix. The precipitates  $(\text{Fe,Cr})_7\text{C}_3$  and  $(\text{Ti,W})\text{C}$  show considerable increase in size and volume fraction after the 1000 °C thermal treatment. The microstructural evolution of the 25 vol.%  $\text{Cr}_3\text{C}_2@ \text{SiC}$ -NFA composite during the SPS sintering and after the thermal treatment can be explained using the ThermoCalc phase diagram and diffusion/precipitation simulations. The coarsening rate of

the precipitates ((Fe,Cr)<sub>7</sub>C<sub>3</sub> and (Ti,W)C) calculated using the ThermoCalc DICTRA module matches well with the experimental results.

### **Acknowledgment**

This work was supported financially by the Office of Nuclear Energy of Department of Energy (No. #DE-NE0008264).

### **References**

- [1] C.R.F. Azevedo, Eng. Failure Anal. 18 (2011) 1943-1962.
- [2] K.L. Murty, I. Charit, J. Nucl. Mater. 383 (2008) 189-195.
- [3] R.B. Rebak, Metall. Mater. Trans. E 2 (2015) 197-207.
- [4] S.J. Zinkle, G.S. Was, Acta Mater. 61 (2013) 735-758.
- [5] A. Kimura, R. Kasada, N. Iwata, H. Kishimoto, C.H. Zhang, J. Isselin, P. Dou, J.H. Lee, N. Muthukumar, T. Okuda, M. Inoue, S. Ukai, S. Ohnuki, T. Fujisawa, T.F. Abe, J. Nucl. Mater. 417 (2011) 176-179.
- [6] G.R. Odette, JOM 66 (2014) 2427-2441.
- [7] G.R. Odette, M.J. Alinger, B.D. Wirth, Annu. Rev. Mater. Res. 38 (2008) 471-503.
- [8] A. Hishinuma, A. Kohyama, R.L. Klueh, D.S. Gelles, W. Dietz, K. Ehrlich, J. Nucl. Mater. 258 (1998) 193-204.
- [9] R.L. Klueh, A.T. Nelson, J. Nucl. Mater. 371 (2007) 37-52.
- [10] A. Kohyama, A. Hishinuma, D.S. Gelles, R.L. Klueh, W. Dietz, K. Ehrlich, J. Nucl. Mater. 233 (1996) 138-147.
- [11] R. Lindau, A. Moslang, M. Schirra, P. Schlossmacher, M. Klimenkov, J. Nucl. Mater. 307-311 (2002) 769-772.
- [12] T. Okuda, M. Fujiwara, J. Mater. Sci. Lett. 14 (1995) 1600-1603.

- [13] S. Ukai, M. Fujiwara, *J. Nucl. Mater.* 307–311 (2002) 749–757.
- [14] Y. Katoh, L.L. Snead, I. Szlufarska, W.J. Weber, *Curr. Opin. Solid State Mater. Sci.* 16 (2012) 143-152.
- [15] K.A. Terrani, B.A. Pint, C.M. Parish, C.M. Silva, L.L. Snead, Y. Katoh, *J. Am. Ceram. Soc.* 97 (2014) 2331-2353.
- [16] L.L. Snead, T. Nozawa, M. Ferraris, Y. Katoh, R. Shinavski, M. Sawan, *J. Nucl. Mater.* 417 (2011) 330-339.
- [17] K. Yueh, K.A. Terrani, *J. Nucl. Mater.* 448 (2014) 380-388.
- [18] G.R. Odette, D.T. Hoelzer, *JOM* 62 (2010) 84-92.
- [19] P. Dubuisson, Y.d. Carlan, V. Garat, M. Blat, *J. Nucl. Mater.* 428 (2012) 6-12.
- [20] S. Ukai, M. Harada, H. Okada, M. Inoue, S. Nomura, S. Shikakura, K. Asabe, T. Nishida, M. Fujiwara, *J. Nucl. Mater.* 204 (1993) 65-73.
- [21] N. Baluc, J.L. Boutard, S.L. Dudarev, M. Rieth, J.B. Correia, B. Fournier, J. Henry, F. Legendre, T. Leguey, M. Lewandowska, R. Lindau, E. Marquis, A. Muñoz, B. Radiguet, Z. Oksiuta, *J. Nucl. Mater.* 417 (2011) 149-153.
- [22] T.S. Byun, J.H. Kim, J.H. Yoon, D.T. Hoelzer, *J. Nucl. Mater.* 407 (2010) 78-82.
- [23] R.B. Rebak, *JOM* 66 (2014) 2424-2426.
- [24] M.P. Brady, Y. Yamamoto, M.L. Santella, L.R. Walker, *Oxid. Met.* 72 (2009) 311-333.
- [25] L. Hallstadius, S. Johnson, E. Lahoda, *Prog. Nucl. Energy* 57 (2012) 71-76.
- [26] B.A. Pint, K.A. Terrani, M.P. Brady, T. Cheng, J.R. Keiser, *J. Nucl. Mater.* 440 (2013) 420-427.
- [27] P. Yvon, F. Carré, *J. Nucl. Mater.* 385(2) (2009) 217-222.

- [28] T. Koyanagi, Y. Katoh, T. Nozawa, L.L. Snead, S. Kondo, C.H. Henager, M. Ferraris, T. Hinoki, Q. Huang, *J. Nucl. Mater.* 511 (2018) 544-555.
- [29] K.A. Terrani, L.L. Snead, J.C. Gehin, *J. Nucl. Mater.* 427 (2012) 209-224.
- [30] Y. Katoh, L.L. Snead, I. Szlufarska, W.J. Weber, *Curr. Opin. Solid State Mater. Sci.* 16 (2012) 143-152.
- [31] J.J. Powers, B.D. Wirth, *J. Nucl. Mater.* 405 (2010) 74-82.
- [32] P.A. Demkowicz, B. Liu, J.D. Hunn, *J. Nucl. Mater.* 515 (2019) 434-450.
- [33] Z. Hu, K. Ning, K. Lu, *Mater. Sci. Eng. A* 670 (2016) 75-80.
- [34] Z. Hu, K. Ning, K. Lu, *Mater. Sci. Eng. A* 682 (2017) 586-592.
- [35] K. Ning, K. Lu, K. Bawane, Z. Hu, *J. Nucl. Mater.* 498 (2018) 50-59.
- [36] K. Ning, H.F. Ju, K. Bawane, K. Lu, *Mater. Sci. Eng. A* 700 (2017) 183-190.
- [37] K. Bawane, K. Ning, K. Lu, *Corros. Sci.* 131 (2018) 365-375.
- [38] K. Bawane, K. Lu, X. Bai, W.Y. Chen, M. Li, *Materialia* 7 (2019) 100412.
- [39] K. Ning, K. Lu, *Compos. Part B* 167 (2019) 746-753.
- [40] C.P. Massey, D.T. Hoelzer, R.L. Seibert, P.D. Edmondson, A. Kini, B. Gault, K.A. Terrani, S.J. Zinkle, *J. Nucl. Mater.* 522 (2019) 111-122.
- [41] H. Kishimoto, M.J. Alinger, G.R. Odette, T. Yamamoto, *J. Nucl. Mater.* 329-333 (2004) 369-371.
- [42] X. Zhou, Y. Liu, L. Yu, Z. Ma, Q. Guo, Y. Huang, H. Li, *Mater. Des.* 132 (2017) 158-169.
- [43] M.A. Auger, V. de Castro, T. Leguey, A. Muñoz, R. Pareja, *J. Nucl. Mater.* 436 (2013) 68-75.
- [44] I. Hilger, X. Boulnat, J. Hoffmann, C. Testani, F. Bergner, Y. De Carlan, F. Ferraro, A. Ulbricht, *J. Nucl. Mater.* 472 (2016) 206-214.

- [45] T.S. Byun, J.H. Yoon, D.T. Hoelzer, Y.B. Lee, S.H. Kang, S.A. Maloy, *J. Nucl. Mater.* 449 (2014) 290-299.
- [46] J.H. Yoon, Y. Lee, S.H. Kang, T.S. Byun, D.T. Hoelzer, *Curr. Nanosci.* 10 (2014) 47-50.
- [47] A. García-Junceda, M. Campos, N. García-Rodríguez, J.M. Torralba, *Metall. Mater. Trans. A* 47 (2016) 5325-5333.
- [48] I. Hilger, F. Bergner, T. Weißgärber, D. Bouvard, *J. Am. Ceram. Soc.* 98 (2015) 3576-3581.
- [49] H. Zhang, Y. Huang, H. Ning, C.A. Williams, A.J. London, K. Dawson, Z. Hong, M.J. Gorley, C.R.M. Grovenor, G.J. Tatlock, S.G. Roberts, M.J. Reece, H. Yan, P.S. Grant, *J. Nucl. Mater.* 464 (2015) 61-68.
- [50] X. Boulnat, M. Perez, D. Fabregue, T. Douillard, M.-H. Mathon, Y. de Carlan, *Metall. Mater. Trans. A* 45 (2013) 1485-1497.
- [51] M. Hernández-Mayoral, M. Serrano, E. Oñorbe, A. García-Junceda, I. Hilger, B. Kloeden, T. Weissgaerber, A. Ulbricht, F. Bergner, B. Radiguet, A. Etienne, A. Shariq, C.D. Dewhurst, *Mater. Sci. Technol.* 30 (2014) 1669-1675.
- [52] Z. Li, Z. Lu, R. Xie, C. Lu, C. Liu, *Mater. Sci. Eng. A* 660 (2016) 52-60.
- [53] R. Xie, Z. Lu, C. Lu, Z. Li, X. Ding, C. Liu, *Fusion Eng. Des.* 115 (2017) 67-73.
- [54] B. Srinivasarao, K. Oh-ishi, T. Ohkubo, K. Hono, *Acta Mater.* 57 (2009) 3277-3286.
- [55] Z.A. Munir, U. Anselmi-Tamburini, M. Ohyanagi, *J. Mater. Sci.* 41 (2006) 763-777.
- [56] J.H. Jang, C.H. Lee, Y.U. Heo, D.W. Suh, *Acta Mater.* 60 (2012) 208-217.
- [57] A. Bjarbo, M. Hattestrand, *Metall. Mater. Trans. A* 32 (2001) 19-27.
- [58] S. Ohtsuka, Y. Yano, T. Tanno, T. Kaito, K. Tanaka, *Mater. Trans.* 54 (2013) 2018-2026.
- [59] A. Schneider, G. Inden, *Acta Mater.* 53 (2005) 519-531.

**Figure list:**

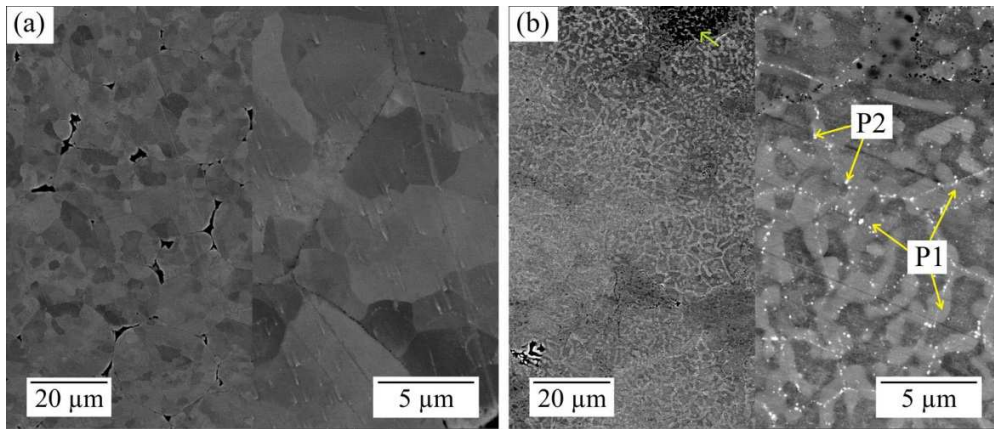


**Fig. 1.** SEM micrographs of (a) NFA and (b) 25 vol.% Cr<sub>3</sub>C<sub>2</sub>@SiC-NFA composite after the SPS sintering (the right side is the magnified image of the left side for each sample).

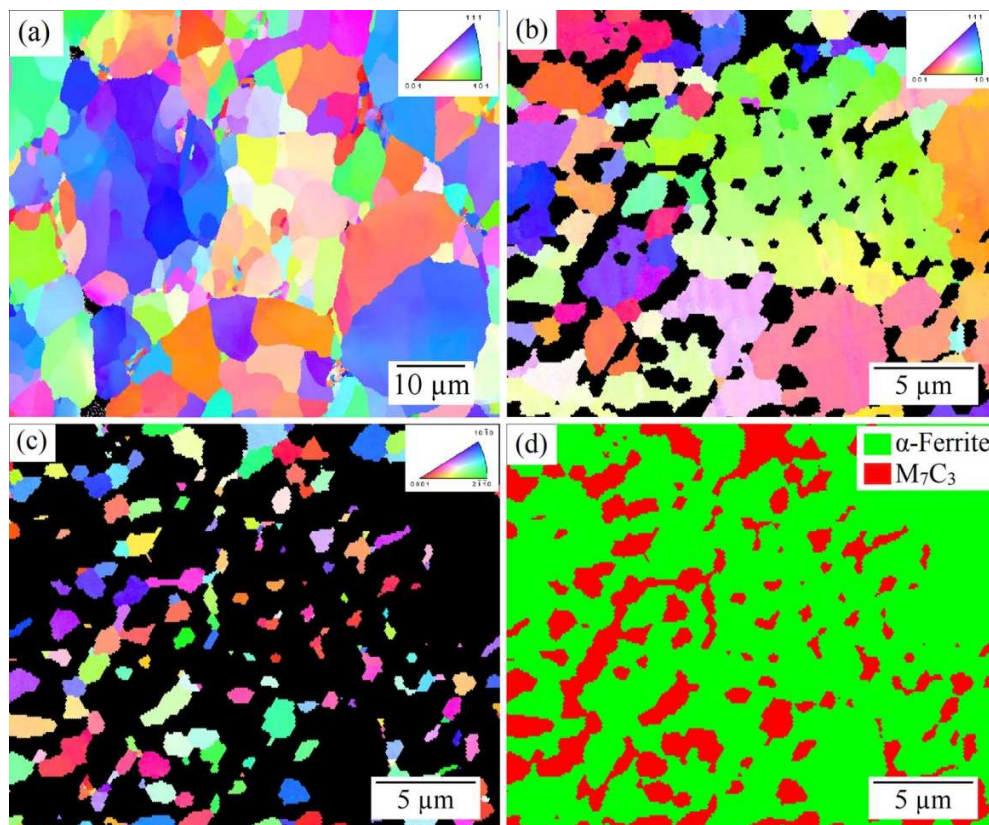


**Fig. 2.** (a) IPF map of the NFA sample; IPF maps of (b)  $\alpha$ -ferrite grains and (c)  $M_7C_3$  grains, and (d) phase map of the 25 vol.%  $Cr_3C_2@NFA-SiC$  composite after the SPS sintering.

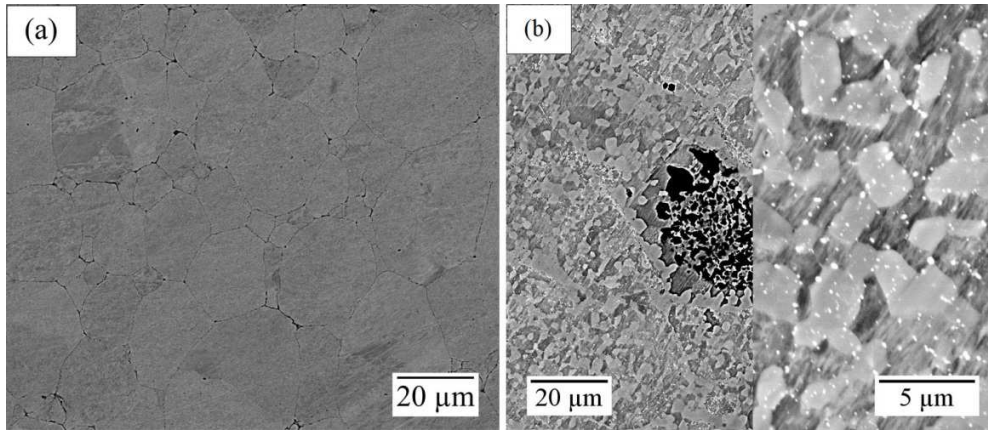


**Fig. 3.** SEM micrographs of (a) NFA and (b) 25 vol.%  $Cr_3C_2@SiC-NFA$  composite after the thermal treatment at 1000°C for 50 hours (the right part is the magnified image of the left part).

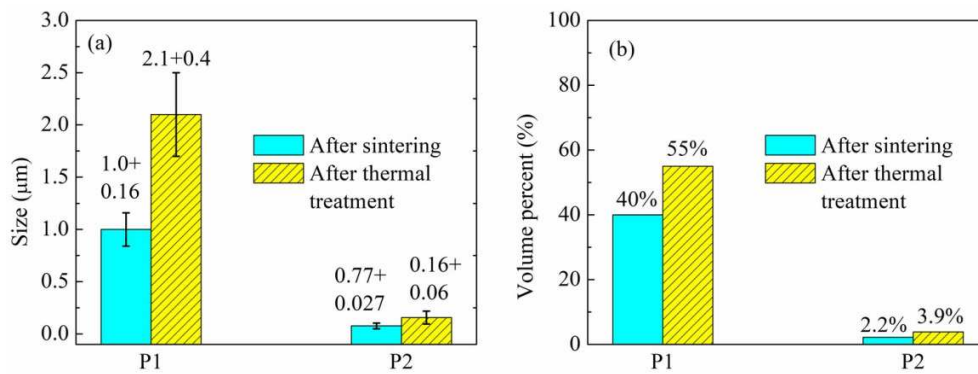


**Fig. 4.** (a) Size and (b) volume fraction of P1 and P2 precipitates before and after the 1000 °C thermal treatment for 50 h.

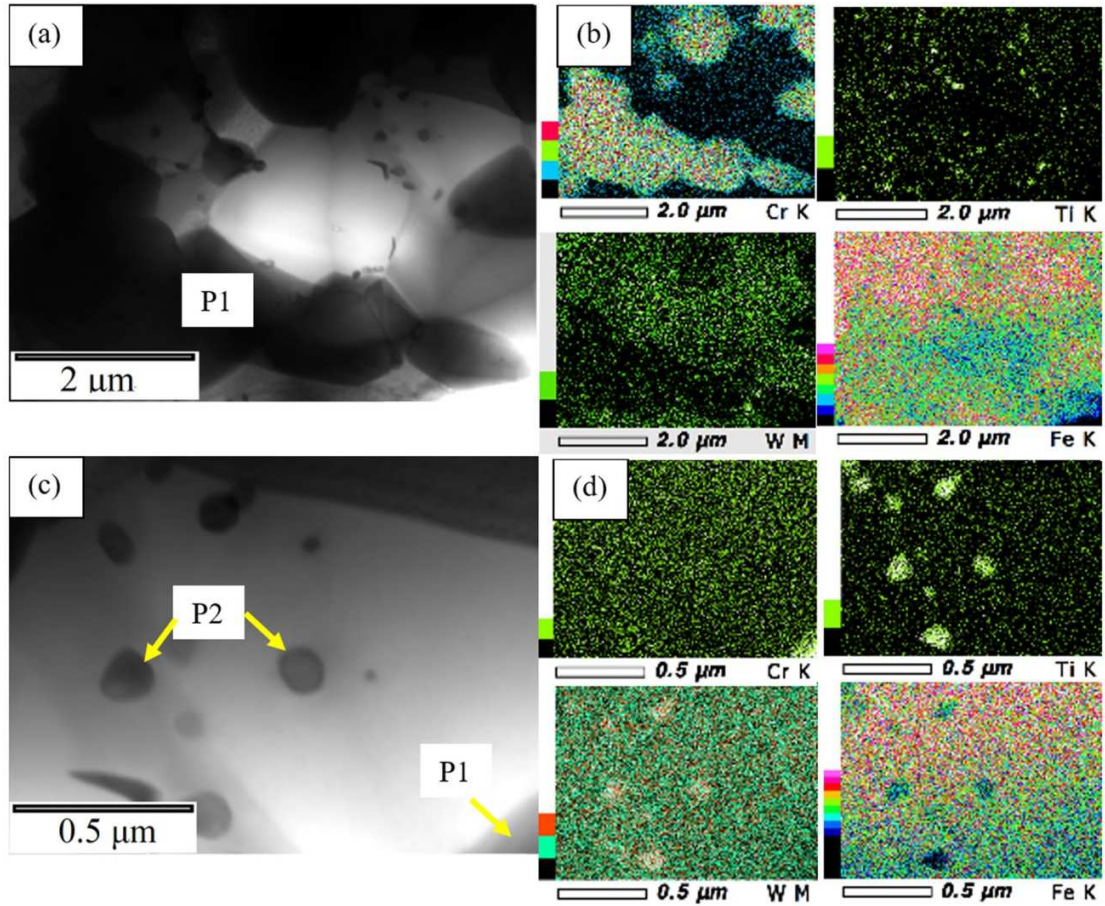


**Fig. 5.** STEM-BF images (a, c) with corresponding EDS mappings (b, d) for the  $\text{Cr}_3\text{C}_2@\text{SiC}$ -NFA composite after the 1000 °C treatment for 50 h.

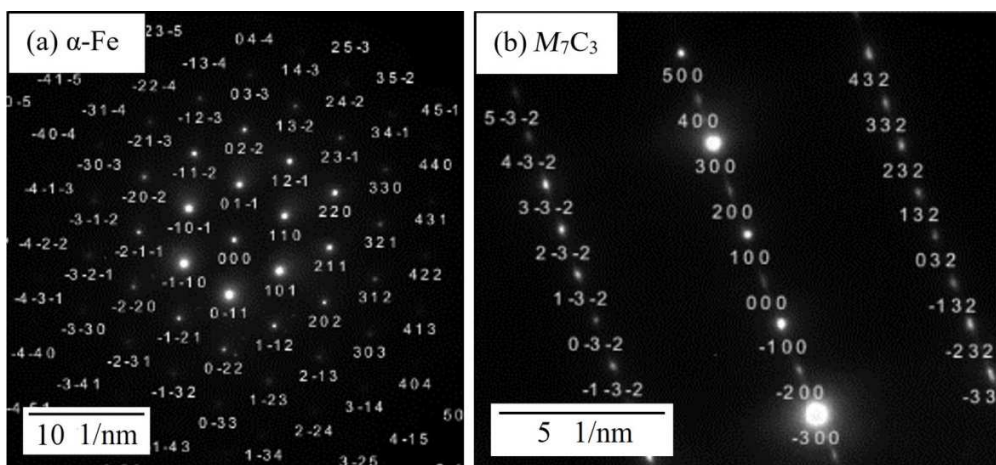


**Fig. 6.** Diffraction patterns from the (a) bright area and (b) dark area (P1) in Fig. 5(a).

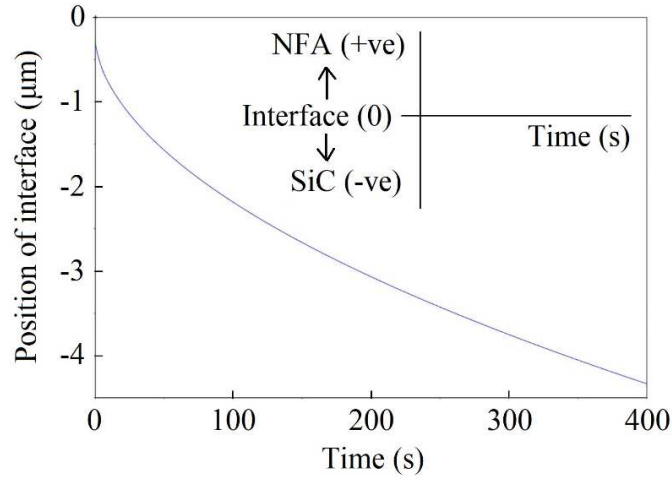


**Fig. 7.** Dissolution kinetics of SiC in the NFA matrix at a sintering temperature of 950 °C.

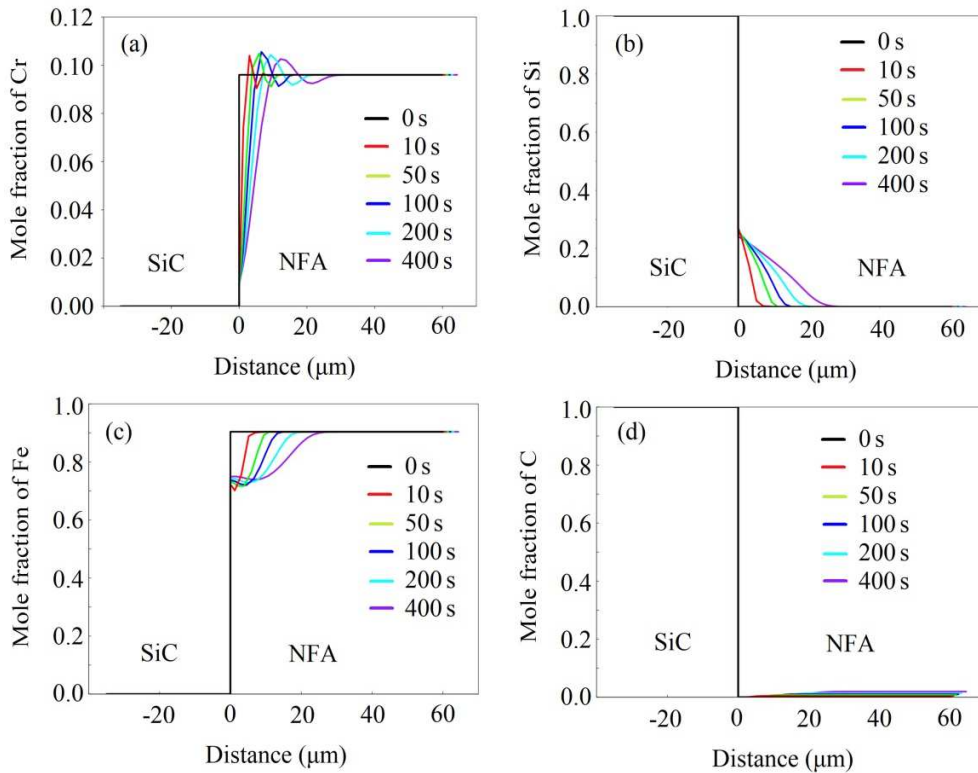


**Fig. 8.** Diffusion behaviors of (a) Cr, (b) Si, (c) Fe, and (d) C based on the ThermoCalc-DICTRA simulations during sintering at 950 °C.

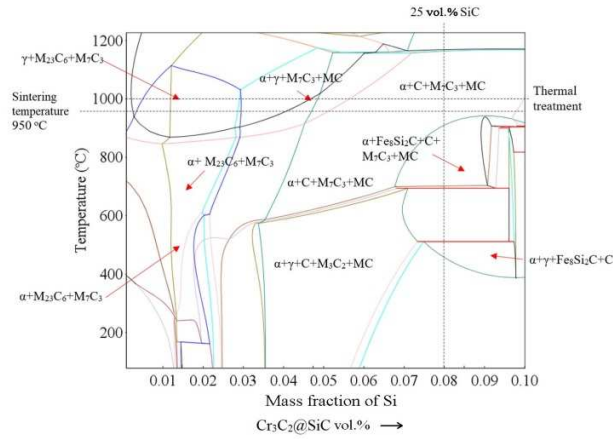


**Fig. 9.** Phase diagram of the  $\text{Cr}_3\text{C}_2@\text{SiC}$ -NFA system.

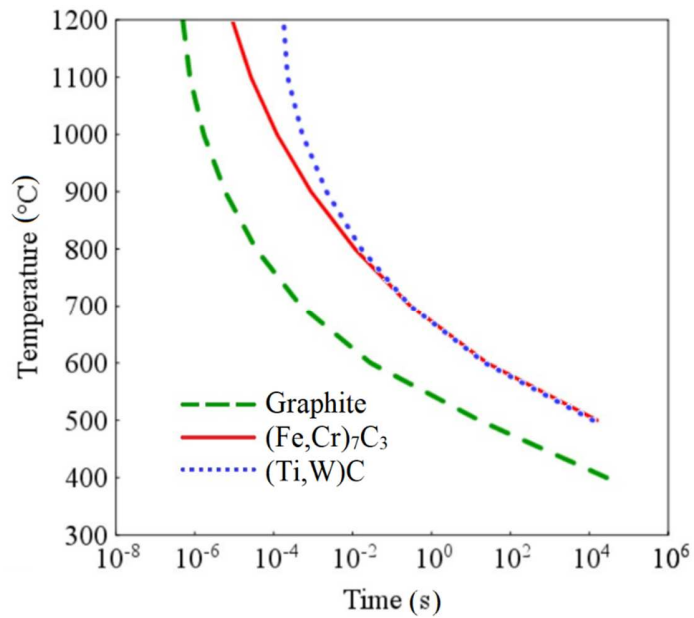


**Fig. 10.** TTT diagram of graphite,  $(\text{Fe,Cr})_7\text{C}_3$ , and  $(\text{Ti,W})\text{C}$  phases for the 25 vol.%  $\text{Cr}_3\text{C}_2@\text{SiC}$ -NFA composite.

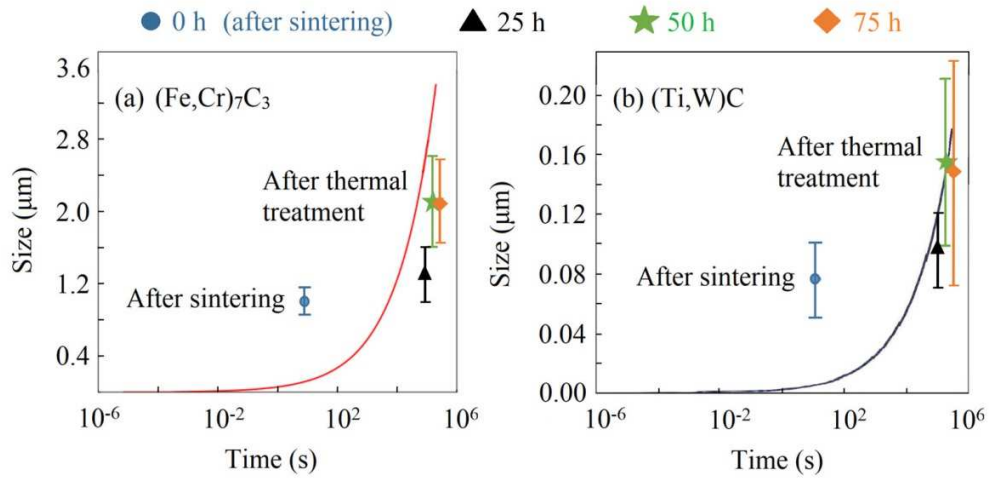


**Fig. 11.** ThermoCalc PRISMA simulations of the size of (a)  $(\text{Fe,Cr})_7\text{C}_3$  and (b)  $(\text{Ti,W})\text{C}$  precipitates and the corresponding experimental values after the sintering and thermal treatment (Data points with error bars show experimental values, which are also reported in Fig. 4(a); curve plots show simulation results).

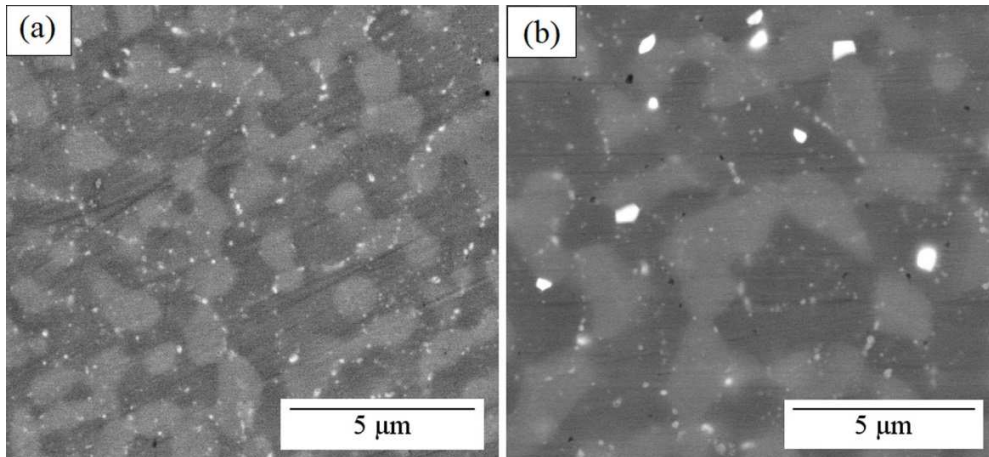


**Fig. 12.** SEM micrographs of  $\text{Cr}_3\text{C}_2@ \text{SiC-NFA}$  composites after thermal treatment at  $1000\text{ }^\circ\text{C}$  for (a) 25 h and (b) 75 h.

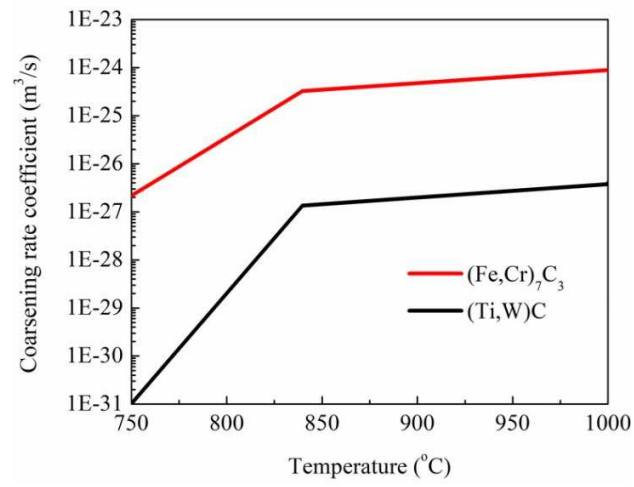


**Fig. 13.** ThermoCalc DICTRA simulations of the coarsening rate coefficient of the  $(\text{Fe,Cr})_7\text{C}_3$  and  $(\text{Ti,W})\text{C}$  precipitates.